

See discussions, stats, and author profiles for this publication at: <https://www.researchgate.net/publication/374475383>

Influence of oxygen vacancies on the lithium-doped Mn:ZnO thin films for improved NO₂ gas-sensing applications

Article in *Journal of Materials Science: Materials in Electronics* · October 2023

DOI: 10.1007/s10854-023-11282-0

CITATIONS

3

READS

130

4 authors, including:



Jasmi K K

St. Thomas College, Thrissur

11 PUBLICATIONS 27 CITATIONS

SEE PROFILE



Siril vs

Cochin University of Science and Technology

16 PUBLICATIONS 69 CITATIONS

SEE PROFILE



K.N. Madhusoodanan


Cochin University of Science and Technology

140 PUBLICATIONS 734 CITATIONS

SEE PROFILE



Influence of oxygen vacancies on the lithium-doped Mn:ZnO thin films for improved NO₂ gas-sensing applications

K. K. Jasmi^{1,*} , T. Anto Johny¹, V. S. Siril², and K. N. Madhusoodanan²

¹Department of Physics, St. Thomas' College, Affiliated to University of Calicut, Thrissur 680001, India

²Department of Instrumentation, Cochin University of Science and Technology, Cochin 682022, India

Received: 29 June 2023

Accepted: 7 September 2023

© The Author(s), under exclusive licence to Springer Science+Business Media, LLC, part of Springer Nature, 2023

ABSTRACT

Herein, the (Zn_{0.97-x}Li_xMn_{0.03})O ($x = 0, 0.01, 0.03$, and 0.05) thin films were prepared on a glass substrate via the sol-gel spin coating technique to study the influence of lithium on Mn-doped ZnO thin films for structural, optical, electrical, morphological, chemical, and NO₂ gas-sensing applications. According to the XRD analysis, all samples display a hexagonal wurtzite crystal structure. A FESEM analysis revealed that the incorporation of lithium into Mn-doped ZnO results in a smaller grain size with more voids than Mn-doped ZnO. Four-probe Hall measurements revealed the n-type conductivity on (Zn_{0.97-x}Li_xMn_{0.03})O ($x = 0$ and 0.01), whereas samples with ($x = 0.03$ and 0.05) exhibited p-type conductivity, which was well explained. XPS and PL spectra confirmed the abundance of surface oxygen vacancies on the prepared sample. It is revealed that interaction between the defect states of lithium and manganese with inherent defect states of ZnO play a crucial role in carrier transfer for the gas-sensing process. In contrast to Mn-doped ZnO, (Zn_{0.96}Li_{0.01}Mn_{0.03})O exhibits smaller grains and a ninefold gas sensitivity (62.01) toward 75 ppm of NO₂ gas at 210 °C toward 75 ppm of NO₂ gas with a rapid response (30 s) and recovery (125 s) time.

1 Introduction

Over the past few years, environmental pollution has become more of our concern as industrial expansion releases harmful gases into the atmosphere at an accelerated rate worldwide. Among the hazardous gases, NO₂ is considered the most toxic, which can cause acid rain and human health-related issues [1–3]. Frequent exposure to NO and NO₂ gas causes acute respiratory distress, as reported by Qureshi et al. [4]. There

are plenty of research work that have been published to identify materials that are suitable for gas-sensing devices. In addition to being more practical to use, the ideal sensing material should be highly capable of detecting gases and be renewable in nature. Designing a reliable NO₂ gas sensor that can detect dangerous gases accurately is crucial for environmental pollution and industry safety regulations. Therefore, developing a susceptible NO₂ gas sensor with a fast response and

Address correspondence to E-mail: jasmifirdhouse@gmail.com

recovery time is imperative for monitoring a healthy environment.

Metal oxide semiconductor (MOS) gas sensors have received much attention due to their low cost, high sensitivity, low working temperature, and affordability. It has been reported that a wide range of MOSs have been investigated for fabricating NO₂ gas sensors. These includes In₂O₃, SnO₂, Fe₂O₃, CuO, NiO, WO₃, ZnO, and Co₃O₄ [5–11]. Among these, researchers have been drawn to n-type ZnO gas sensors owing to their remarkable gas-sensing response, ease of fabrication, large band gap, and high exciton binding energy. Since it is a surface-dependent gas-sensing material, the oxygen adsorption rate and particle size are crucial factors in ZnO nanostructures. A unique fabrication technique or doping/co-doping with a suitable element enhances gas-sensing capabilities by modifying the shape and surface-to-volume ratio of ZnO.

According to the literature review, transition metal-doped ZnO gas sensors are frequently reported as highly sensitive and stable, which include Cu, Ni, Co, Mn, Cr, and Fe [3, 12–16]. Among the transition metals, Mn-doped ZnO seems to be a promising material for enhanced NO₂ gas-sensing applications [3]. Along with this, alkali metal (Li) is also utilized as a dopant for further enhanced gas-sensing application in ZnO [17, 18]. The defect density in ZnO thin films doped with Li can be tuned based on Li concentration for enhanced NO₂ gas sensing [19]. Furthermore, Li can be co-doped with Mn in ZnO to provide photocatalytic functions, ferroelectric properties, and ferromagnetism [20–25]. Numerous investigations have been reported on an assortment of fabrication techniques, including chemical vapor deposition, hydrothermal, SILAR method, co-precipitation, atomic layer deposition, sputtering, sol–gel spin coating process, spray pyrolysis, and pulsed laser deposition. One of these techniques, sol–gel spin coating, attracts the most attention since it is easy to use, requires low temperatures and precise thickness controls, produces homogeneous films, is cost-effective, incorporates additives, and is environmentally friendly.

In this article, we explore the impact of lithium on the structural, electrical, and optical properties of Mn-doped ZnO for enhanced NO₂ gas-sensing applications. The (Zn_{0.97-x}Li_xMn_{0.03})O ($x = 0, 0.01, 0.03, \text{ and } 0.05$) thin films were fabricated via sol–gel spin coating technique. All deposited samples were characterized through XRD,

FESEM-EDX, XPS, Four-probe Hall measurements, UV–Vis spectroscopy, and Photoluminescence. Several parameters associated with gas sensing are also discussed, such as the optimal temperature, concentration-dependent gas response, stability, selectivity, and reproducibility. Among them, the (Zn_{0.96}Li_{0.01}Mn_{0.03})O thin film exhibits superior gas sensitivity with quick response and recovery time toward NO₂ gas at its working temperature of 210 °C.

2 Experimental details

2.1 Materials

The following ACS-grade chemicals were utilized in the synthesis: diethanolamine (DMA), zinc acetate dihydrate, and isopropyl (IPA) were bought from Merck, India. Both manganese acetate tetrahydrate and lithium acetate dihydrate were purchased from Sigma-Aldrich, India.

2.2 Fabrication of thin films

The precursor solution (0.5 M) of (Zn_{0.97-x}Li_xMn_{0.03})O ($x = 0, 0.01, 0.03, \text{ and } 0.05$) thin film abbreviated as ML-0, ML-1, ML-3, and ML-5, respectively, was prepared via sol–gel spin coating method. The solution for ML samples was prepared by adding the required amounts of DMA (stabilizer) and zinc acetate dihydrate into the 20 mL of IPA (solvent) and stirred to get a clear solution. Then, add the necessary amount of manganese acetate tetrahydrate and stir until the solution becomes transparent. Finally, add the required quantity of lithium acetate dehydrate to get a transparent solution. After being kept for 48 h to assure stability, the prepared solution was spin coated to a glass substrate, dried for 20 min at 150 °C in a hot-air oven, and then annealed for 30 min at 500 °C in a tube furnace [26]. As a result of proper annealing, the XRD peaks become more intense, the absorption edge shifts, the intensity of photoluminescence emissions is increased, and gas sensors are more sensitive by improving the surface-to-volume ratio, thus increasing the potential for gas adsorption and desorption reactions [27].

2.3 Characterization

The crystalline structure studies were carried out by X-ray diffractometer (PAN Analytical, Japan, $\lambda = 0.154$ nm with Cu-K α radiation), surface morphology was collected from FESEM Carl Zeiss Supra, 40 VP), and chemical state of elements obtained from XPS (Kraton, Axis Ultra). Electrical parameters of the thin films were measured at RT by a four-probe Hall measurement system, HMS-3000, Ecopia, S. Korea. Utilizing a Horiba Fluorolog F3-22 spectrometer to observe photoluminescence spectra, UV-Visible transmission spectra were recorded from a UV-Visible/NIR spectrometer (V-780, JASCO).

2.4 Gas-sensing analysis

An indigenously built gas sensor system was used to investigate NO₂ gas-sensing behavior of the prepared samples at its operating temperature for concentrations ranging from 5 to 75 ppm. Prior to take data, the gas-sensing setup was pre-heated at 500 °C to ensure a moisture-free environment for gas-sensing measurements [28]. The electrical connections are made with two copper wires on thin film, separated by one cm, connected with silver paste on the surface of the thin film. The sensing chamber was fabricated with stainless steel and the setup consists of a gas inlet and outlet parts. A known amount of test gas was injected into the chamber using a syringe to determine the resistance of the sensor film as a function of time. Electrical resistance was recorded using a Keysight 34461A (6.5-resolution) multimeter connected to the test container at a specific atmospheric pressure. After different test gas concentrations were inserted into the gas-sensing device, the gas sensitivity (S) is defined as follows [29, 30].

For oxidizing gas

$$S = \frac{R_g}{R_a} \tag{1}$$

And for reducing gas

$$S = \frac{R_a}{R_g} \tag{2}$$

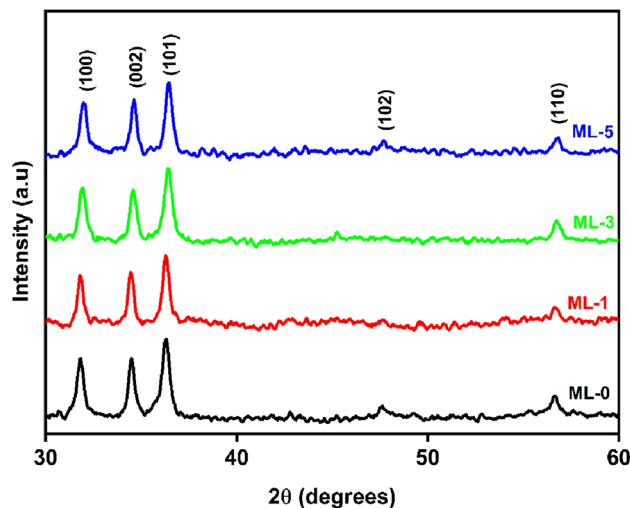


Fig. 1 XRD pattern of ML samples

Table 1 XRD parameters of ML samples

Sample	Lattice constant (Å)		Crystallite size (nm)	Volume (Å) ³	Lattice strain (10 ⁻³)
	<i>a</i>	<i>c</i>			
ML-0	3.0327	5.2527	38.79	41.8356	1.558
ML-1	3.0372	5.2606	28.08	42.0246	1.67
ML-3	3.0219	5.2341	29.74	41.3934	1.516
ML-5	3.0173	5.2261	32.23	41.2039	1.269

3 Results and discussion

3.1 XRD analysis

XRD analysis revealed that ML sensors exhibit a hexagonal wurtzite structure with phase group p6₃mc, which corresponds precisely with JCPDS card no. 043-0002, and no extra peaks were observed related to Li-O or Mn-O impurities, Fig. 1. The structural parameters in Table 1 demonstrates that the incorporation of Li into Mn-doped ZnO causes lattice expansion up to 1 wt% of Li, indicating interstitial substitution [20]. Additionally, lithium ions make Mn-doped ZnO crystallites smaller than ML-0 due to the structural instability brought on by the effective introduction of the (Mn-Li) co-dopant into the ZnO lattice [31, 32]. ML-1 has smaller grain sizes, so more grain boundaries are expected per unit volume, increasing lattice strain, Table 1 [33]. Lattice constants *a* and *c* are calculated using the following equations.

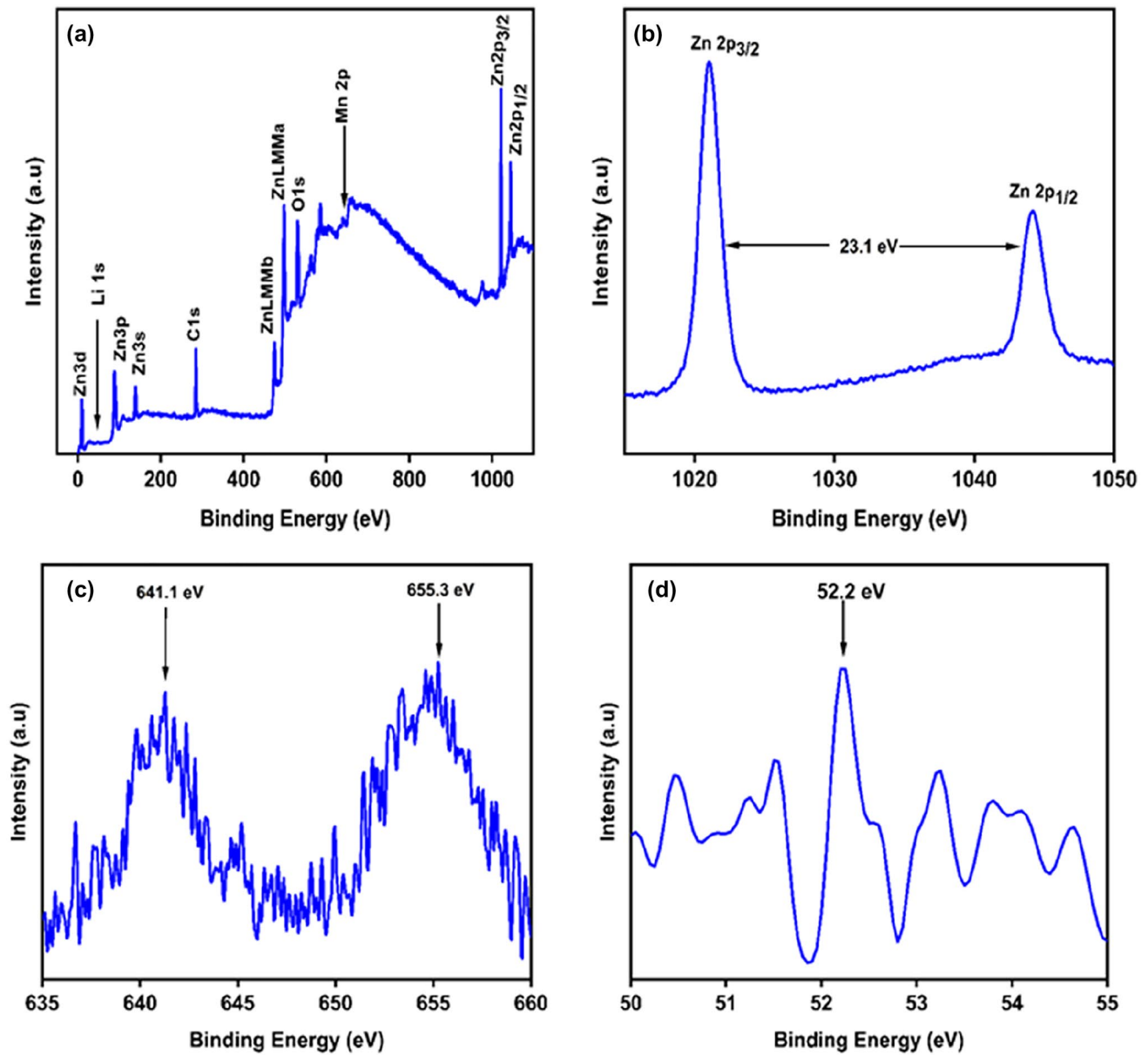


Fig. 2 Scan for **a** survey, **b** Zn2p, **c** Mn 2p, and **d** Li 1s spectrum

$$a = \frac{\lambda}{\sqrt{3}\sin\theta} \tag{3}$$

$$c = \frac{\lambda}{\sin\theta} \tag{4}$$

The crystallite size (D) using the Debye–Scherrer formula,

$$D = \frac{0.9\lambda}{\beta\cos\theta}. \tag{5}$$

Volume (V) is calculated as follows:

$$V = \frac{\sqrt{3}a^2c}{2} = 0.866a^2c. \tag{6}$$

And the lattice strain of a thin film is calculated using the formula given below:

$$\varepsilon = \frac{\beta\cos\theta}{4}, \tag{7}$$

where θ is the Bragg’s angle, λ is the X-ray wavelength, and β is the full width at half maximum (FWHM).

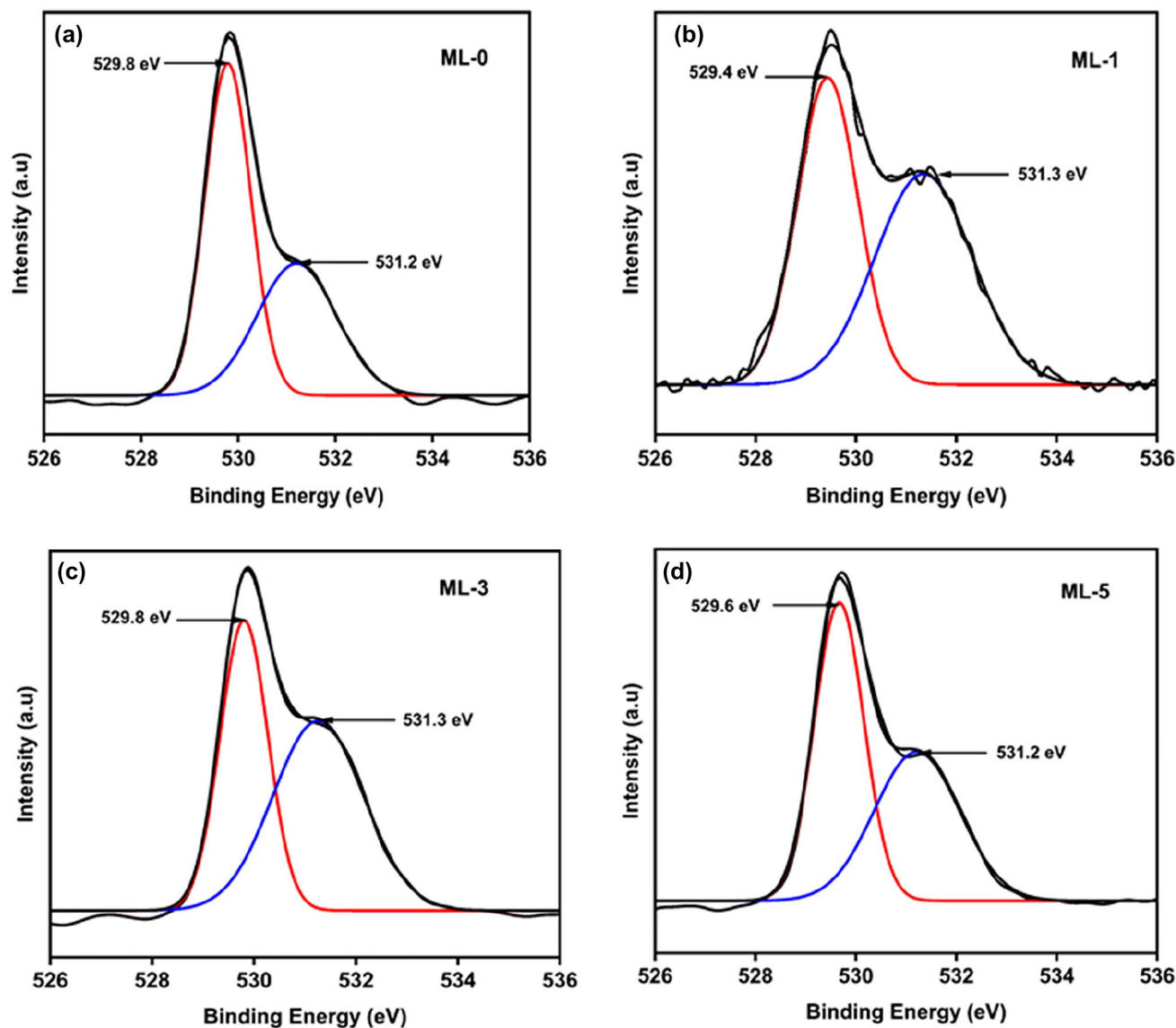


Fig. 3 a-d O 1s XPS spectra of ML samples

3.2 XPS analysis

The XPS analysis is performed to ascertain the chemical bonding and elemental composition state of the ML samples. For more clarity, Zn 2p, Mn 2p, Li 1s, and O 1s spectra were recorded using high-resolution XPS spectra. Only Zn, O, C, Mn, and Li peaks were seen in the XPS survey scan of the ML sample, as shown in Fig. 2a, indicating the purity of the sample. According to the Zn 2p XPS spectra Fig. 2b, the peak corresponding to $2p_{3/2}$ and $2p_{1/2}$ were located at 1021.1 eV and 1044.2 eV, respectively. The binding energy difference was 23.1 eV; this indicates Zn exists as Zn^{2+}

in the ZnO matrix. The Mn 2p spectra exhibited two peaks at 641.1 eV and 655.3 eV associated with $2p_{3/2}$ and $2p_{1/2}$, respectively, revealing that Mn exists as $a + 2$

Table 2 Oxygen defect and gas-sensing parameters of ML samples

Sample	O_L (%)	O_V (%)	Gas response ($\frac{R_g}{R_a}$)	Response time (s)	Recovery time (s)
ML-0	62.14	37.86	7.2	102	203
ML-1	44.62	55.38	62.01	30	125
ML-3	46.99	53.01	33.7	47	145
ML-5	53.69	46.31	31.4	52	187

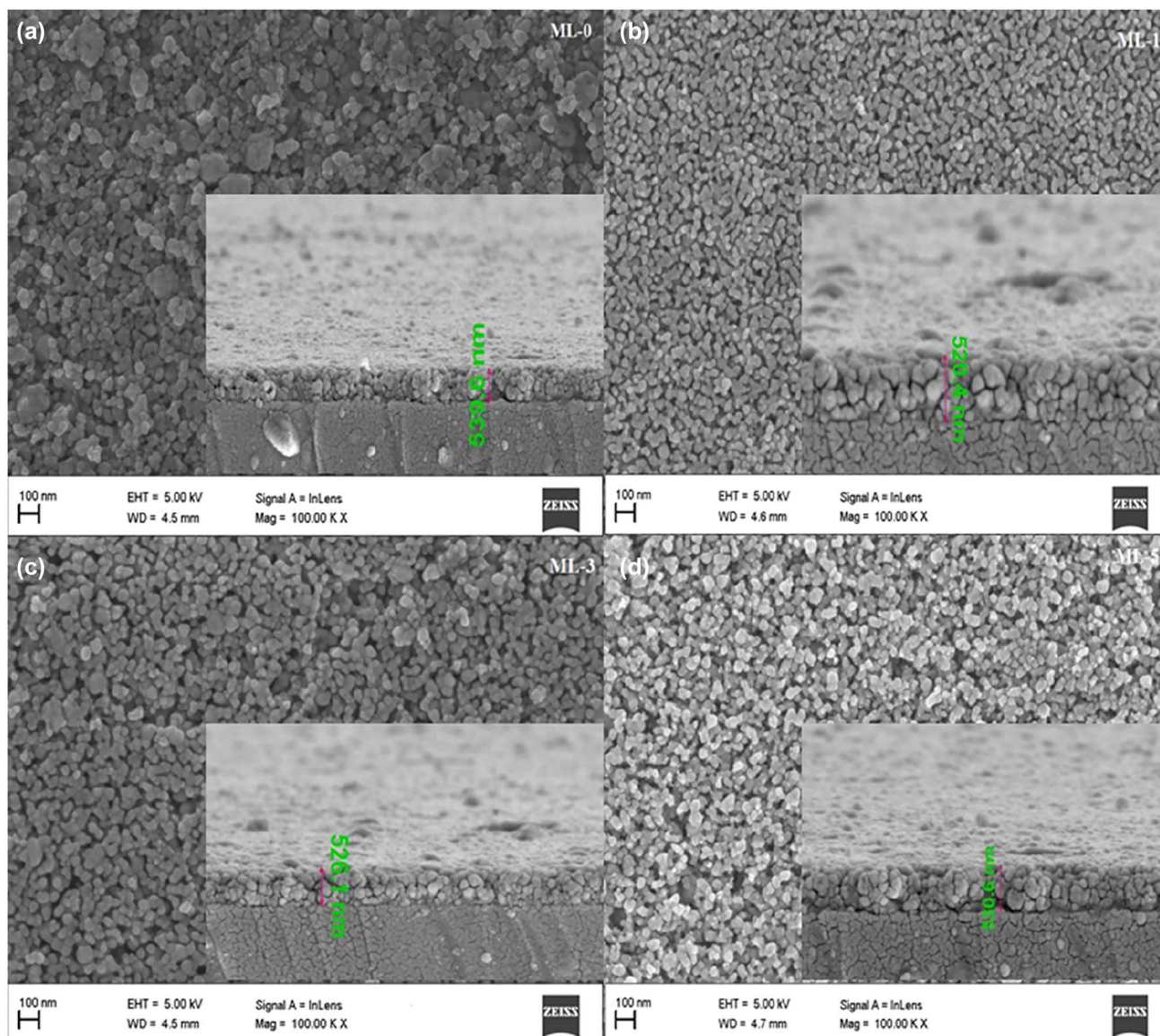


Fig. 4 FESEM images of ML samples **a** ML-0, **b** ML-1, **c** ML-3, and **d** ML-5

oxidation state in ZnO, Fig. 2c [34]. The Li 1s spectra of ML-1, with a 52.2-eV binding energy, also confirm the successful incorporation of Li into the ML-1 sample, Fig. 2d [35–37].

A XPS spectrum of O 1s for ML samples was collected in order to study oxygen vacancies in more detail. It consists of two Gaussian peaks—one centered at 529 eV associated with lattice oxygen (O_L), such as Mn–O, Li–O, and Zn–O, and the other at 531 eV attributed to oxygen vacancy zones (O_V), Fig. 3a–d, Table 2. Among the prepared samples, the ML-1 sample resulted in notable increases in oxygen vacancies

(O_V), which is predicted to indicate more significant gas sensitivity.

3.3 FESEM analysis

The morphological impact of Li on Mn:ZnO was observed through FESEM analysis, Fig. 4a–d. The incorporation of Li into Mn-doped ZnO results in formation of more interspaces and voids both spherical and irregular grains that are uniformly dispersed, with grain size ranging from 32.75 to 41.41 nm. Voids provide an additional surface area for gas molecules to interact with the sensing

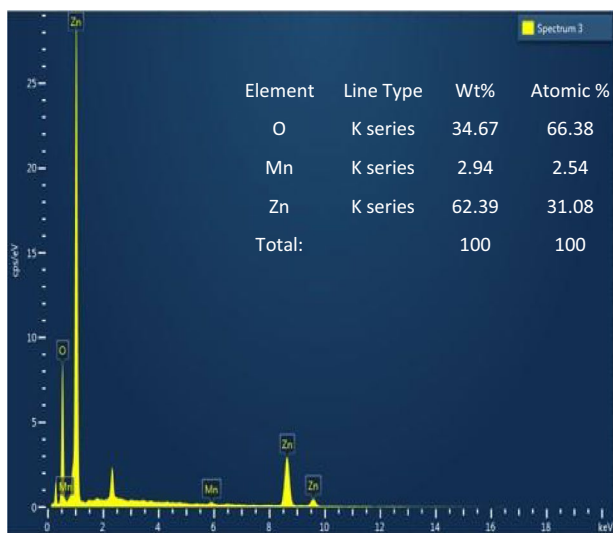


Fig. 5 EDX image of ML-1 sample

material and create pathways for gas molecules to diffuse through the material selectively and trap specific gas molecules based on size and chemical interactions, enhancing the material ability to detect target gas accurately. The small grain size and more voids with a smooth surface observed in ML-1 sample may have been caused by Mn and Li disrupting the growth process, as described in earlier investigations [38]. When the concentration of Li increases, agglomeration is observed, possibly because of variations in surface energy due to local inhomogeneity in dopant distribution. The thickness of ML samples, as determined by FESEM cross-sections ranges 520.4 to 539.6 nm, is displayed in the inset of Fig. 4a–d. The elemental distribution of the ML-1 sample, as shown in Fig. 5, was further verified by EDX analysis. Li is not visible due to its low atomic number; only peaks related to zinc, oxygen, and manganese are observed [39].

3.4 Electrical analysis

In order to study the electrical properties of Li on Mn:ZnO, the dopant concentration of Li varies as 1 wt%, 3 wt%, and 5 wt%. Mn-doped ZnO shows n-type conductivity due to oxygen vacancies acting as shallow donors [25]. The incorporation of Li into Mn-doped ZnO varies the conductivity from n-type to p-type. Since Li^+ has a smaller atomic radius than Zn^{2+} , it serves both as a donor and an acceptor. As Li occupies the interstitial site, it acts as a donor,

reducing electrical resistivity and increasing carrier concentration as per the following equation [40].



Kröger–Vink notation describes the generation of holes when lithium is at the substitutional position as follows:



In the Mn-doped ZnO with a low lithium concentration, Mn and Li may form defect complexes ($\text{Mn}'_{\text{Zn}} - \text{Li}'_{\text{Zn}}$), which results in increasing conductivity and decreasing electrical resistance showing n-type conductivity [25]. As Li concentration increases, resistivity increases due to the formation of holes and the recombined electrons resulting in higher resistance and results in p-type conductivity [24]. Sometimes excess manganese ions are trapped near the grain boundary to oppose the charge transfer. The specific conductivity type and its characteristics depend on the doping concentration and the balance between the acceptor and donor dopants, Table 3.

3.5 Spectral analysis

The transmittance spectra are used to investigate the spectral properties of the ML samples. The reduction in particle size caused by an increase in grain boundaries reduces transmittance and reaches a minimum value at ML-1, Fig. 6a [41]. All ML samples exhibit sharp absorption edges, as shown in Fig. 6b, resulting in a red shift of the absorption edge in ML-1. The absorption coefficient (α) has been calculated using the following relationship:

$$\alpha = \left(\frac{1}{t}\right) \ln\left(\frac{1}{T}\right), \quad (10)$$

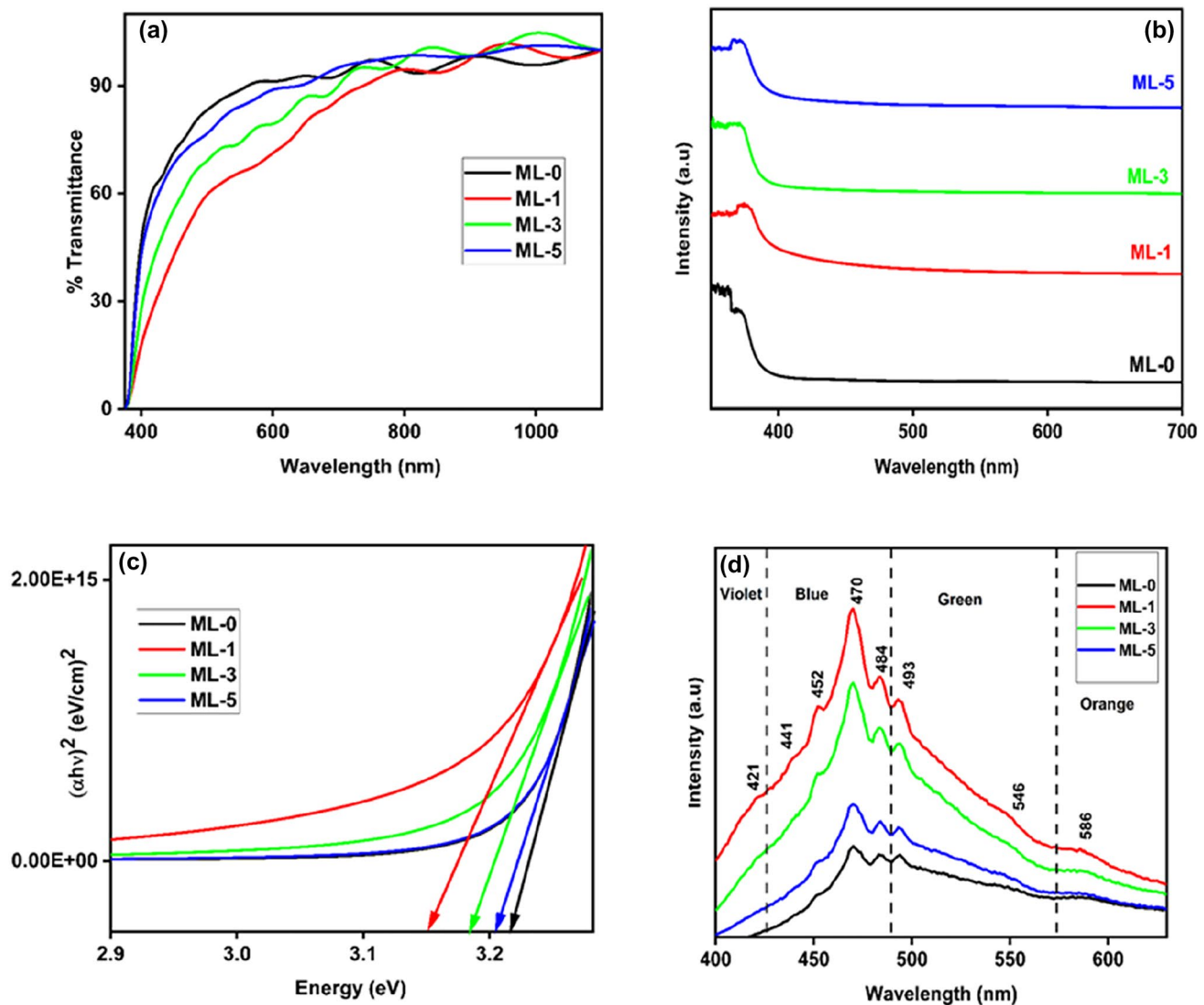
where t is the thickness of the ML samples and T is the transmittance. The following equation shows the relationship between incident photon energy ($h\nu$) and the absorption coefficient (α).

$$(\alpha h\nu) = k(h\nu - E_g)^n, \quad (11)$$

where E_g is the optical band gap of the material, α is the absorption coefficient, k is a constant that depends on the absorption rate, and the value of n for direct

Table 3 Electrical and optical parameters

Sample	Carrier concentration (cm ³)	Resistivity (Ω.cm)	Mobility (cm ² /Vs)	Carrier type	Band gap (eV)
ML-0	1.7×10^{15}	67.6	293.01	n	3.21
ML-1	4.88×10^{14}	43.7	543.6	n	3.15
ML-3	7.97×10^{14}	544	145.02	p	3.18
ML-5	1.52×10^{13}	9310	44.31	p	3.2

**Fig. 6** a Transmission, b absorption, c Tauc plot, and d Photoluminescence spectra of ML samples

allowed transition is $\frac{1}{2}$. The direct band gap of pure and doped ZnO is estimated from Tauc plot as shown in Fig. 6c. Incorporation of dopants enhances the defect in ZnO films, resulting a decrease in E_g from 3.22 to 3.15 eV, with a minimum value for ML-1, Table 3 [42].

Due to the s – p and p – d exchange interaction, the conduction band edge is shifted downward, often reducing the band gap [43]. To determine the changes in the defect states of ZnO with doping, further PL investigations were carried out.

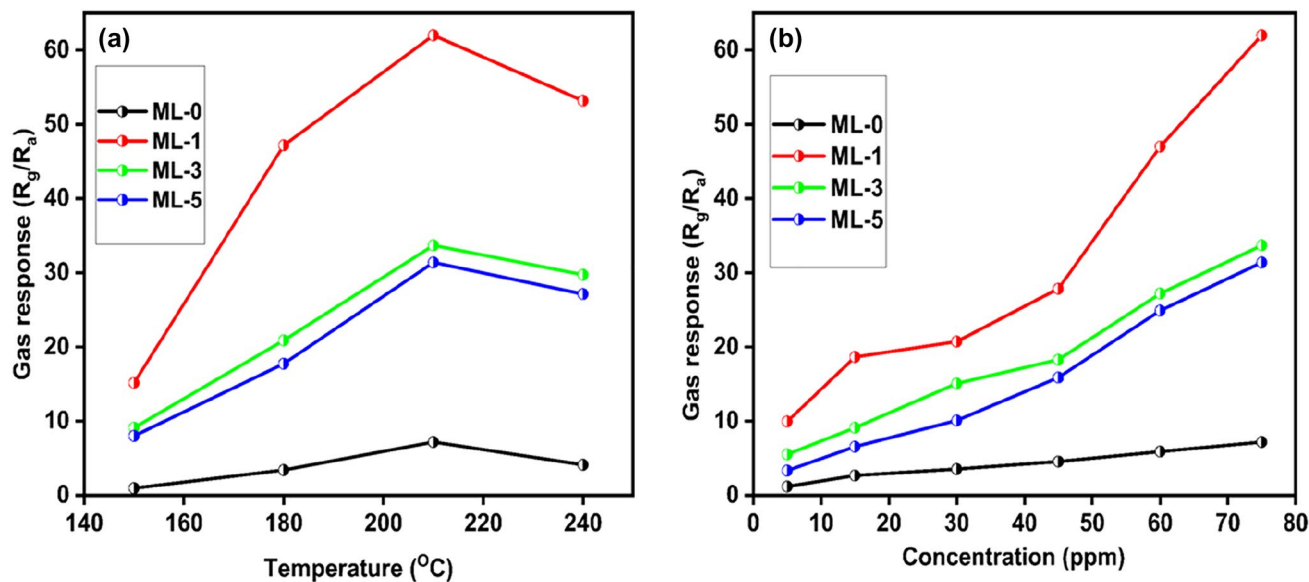


Fig. 7 **a** Sensitivity–Temperature plot and **b** Dynamic Response–time graph

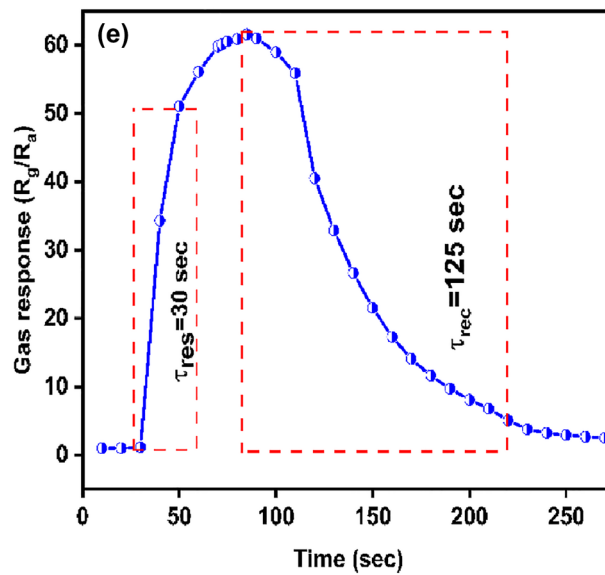
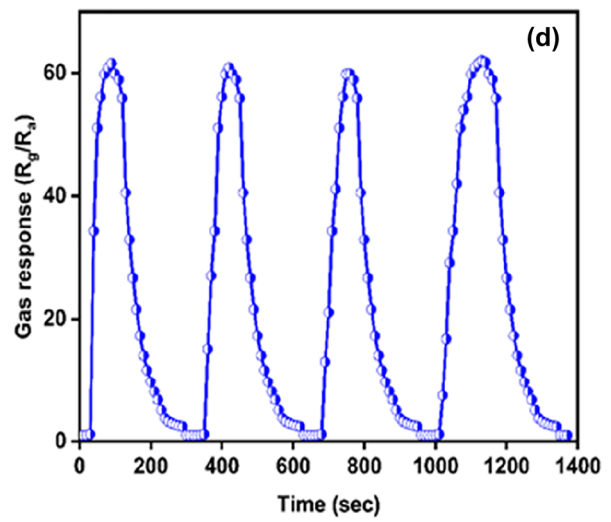
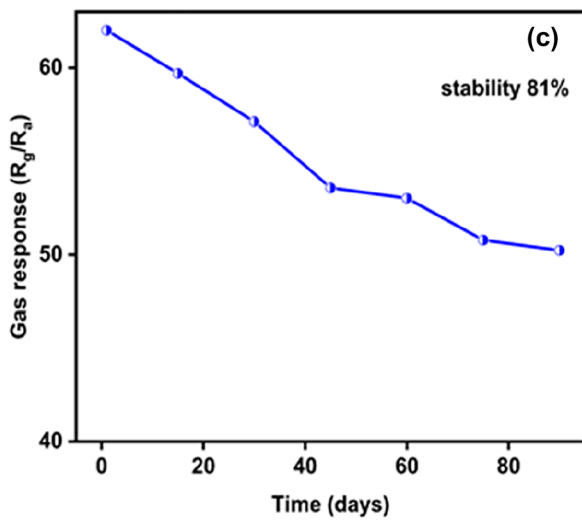
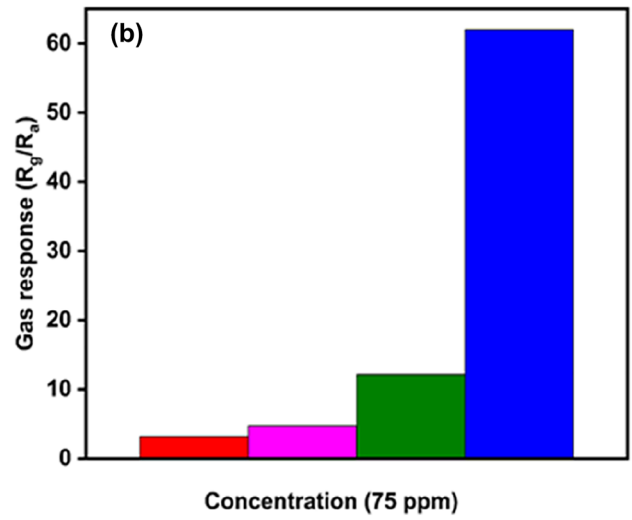
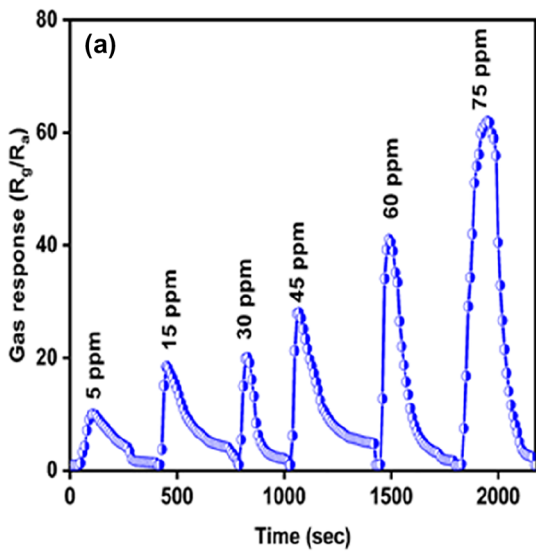
In the present study, photoluminescence spectra of ML samples were excited at 325 nm, as in Fig. 6d. Blue emission is caused by electrons trapped at shallow levels of Zn_i recombining with holes trapped at Zn_v (441–484 nm) [44]. However, the peak at 493 can be attributed to the recombination of photo-generated holes and oxygen vacancies that have been singly ionized [36]. Additionally, the peak at 546 nm results from inherent oxygen vacancies in ZnO [45]. The orange luminescence at 586 nm is attributed to the transition $1^4T \rightarrow 1^6A$ within the Mn 3d-3d sub-shell [25, 34]. Here, the emission intensity increases and reaches a maximum for ML-1. Further increases in the concentration of Li dopant into Mn-doped ZnO decreases the emission peak intensity due to the formation of $Mn_{Zn}^{2+}-Li_{Zn}^{+}$ Complex [25]. The PL spectra reveal that incorporating Li into Mn enhances or creates more defect states, which are expected to be beneficial for gas-sensing response.

3.6 Gas-sensing analysis

The efficiency of a gas sensor depends on an optimum temperature in which the highest gas-sensing response was observed. The gas-sensing response of ML samples toward 75 ppm of NO_2 gas as a function of temperature was studied, as shown in Fig. 7a. It has been observed that the NO_2 gas sensitivity of ML samples increases with temperature and show its maximum at 210 °C, then gradually declines [46]. At the optimal

temperature of 210 °C, the adsorption rate and desorption rates are equal; hence ML samples exhibit the maximum gas-sensing response at this temperature. Low temperatures reduce the sensor's ability to bind NO_2 , and high temperatures efficiently limit the sensor's ability to detect gases due to the rate of gas molecule diffusion. Following exposure to NO_2 gas at different concentrations ranging from 5 to 75 ppm, the gas-sensing responses of the ML samples were examined, Fig. 7b. Concentration-dependent gas sensing is observed in all ML samples. Among them, ML-1 demonstrates the remarkable NO_2 gas-sensing response of 62.01 with a short response (30 s) and recovery (125 s) time. In short, the ML-1 sample is a suitable candidate for further gas-sensing study.

The NO_2 gas-sensing response of the ML-1 sensor for various NO_2 gas concentrations are measured (5 ppm–75 ppm) as in Fig. 8a. Then the selectivity ML-1 toward various gases like Cl_2 , NO, NH_3 , and NO_2 gases with 75 ppm concentration studied. Among them, the sample show exceptional gas sensitivity toward NO_2 gas, as shown in Fig. 8b. Additionally, the ML-1 sample's stability was evaluated and revealed almost identical stability over a three-month period, as shown in Fig. 8c. Furthermore, ML-1 samples exposed continuously to 75-ppm test gas show a steady response up to four consecutive cycles, as shown in Fig. 8d. The response and recovery duration for the ML-1 sensor were determined and demonstrated in

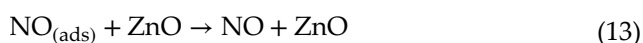
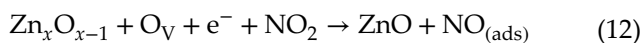


◀Fig. 8 **a** Dynamic response–time curve, **b** Selectivity study toward various toxic gases, **c** Stability measure, **d** Reproducibility, and **e** Response–recovery time for ML-1 sensor

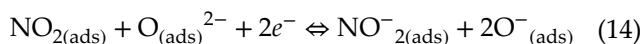
Fig. 8e. The result shows that ML-1 sample is ideal for sensing device applications. Table 4 provides an overview of the contrast studies of several dopants on ZnO thin films for NO₂ gas-sensing performance.

3.7 Gas-sensing mechanism

In MOS-based gas sensors, oxygen vacancies play a key role in gas-sensing mechanisms [50]. The inherent defect states of ZnO are favored by the adsorption site for the test gas. This could be explained using the following Eqs. (12) and (13) [50–52].



In an air-exposed ML sample, oxygen molecules adsorb on the surface, and chemisorbed oxygen anions are formed by withdrawing electrons from the conduction band. This results in the formation of a depletion zone and improves sample resistance [19]. When NO₂ gas is introduced, it interacts with the previously adsorbed O²⁻ as illustrated in Eq. (14).



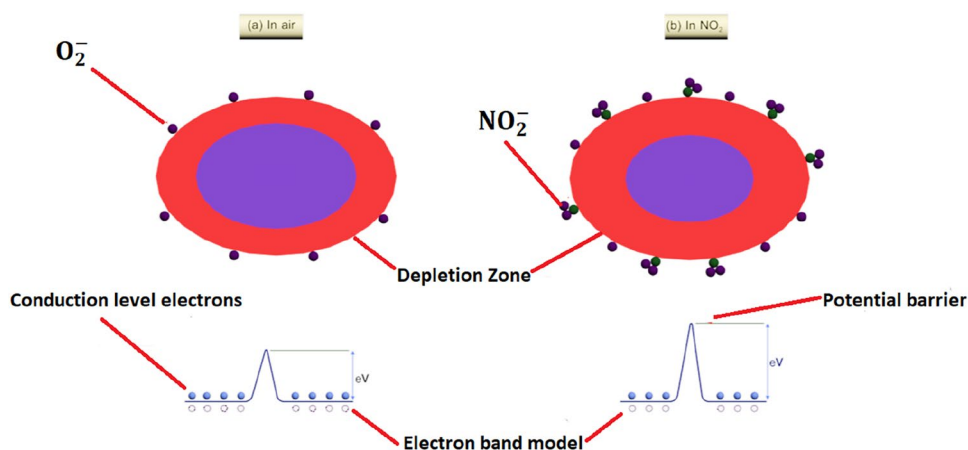
As a result, a potential barrier is formed with a positive charge in the semiconductor and a negative charge on the adsorbed gases. In the presence of NO₂ gas, the barrier height is enlarged due to the extraction of extra electrons from the thin-film sensor surface, increasing sensor resistance. Here, the ML-1 sensor shows outstanding NO₂ gas-sensing performance as Li incorporation into Mn-doped ZnO modifies its surface oxygen vacancies as confirmed by XPS and PL results, Table 2. The energy levels of substituted Li⁺(0.09 eV) and Mn²⁺(0.31 eV) in ZnO possibly formed just below CBM are closely associated with each other [53–56]. As a result, the interaction

Table 4 Gas-sensing response comparative study toward NO₂ gas

Materials	Gases	Con(ppm)	Preparation-method	Gas response	Refs
Cu:ZnO	NO ₂ , H ₂ S, Cl ₂ , SO ₂	100	Co-precipitation	326%*	[47]
Ni:ZnO	NO ₂ , H ₂ S, Cl ₂ , SO ₂	100	Co-precipitation	356%*	[48]
Co:ZnO	NO ₂ , C ₂ H ₅ OH, H ₂ S, Cl ₂ , SO ₂	100	Co-precipitation	286%*	[14]
Fe:ZnO	NO ₂ , CO ₂ , SO ₂ , LPG, Acetone	100	hydrothermal	209.8**	[49]
Mn:ZnO	–	40	hydrothermal	152.3%*	[3]
Li:ZnO	NO ₂ , NH ₃	75	Sol–gel spin coating	34.74**	[19]
Li-Mn:ZnO	NO, NO ₂ , Cl ₂ , NH ₃	75	Sol–gel spin coating	62.01**	Present work

*Gas response = $\frac{R_g - R_a}{R_a} \times 100\%$, **Gas response = $\frac{R_g}{R_a}$

Fig. 9 Pictorial representation of gas-sensing mechanism



between the defect states created by the dopants (Li, Mn) and the intrinsic defects of ZnO supplement each other. Thus, Li facilitates an effective interaction path for transferring charge carriers among defect states in Mn-doped ZnO, resulting increased gas sensitivity. In conclusion, adding optimum quantity of Li to Mn-doped ZnO would increase the sensitivity of the NO₂ gas sensor without disturbing the structure, enabling the development of an effective NO₂ gas detector. The pictorial representation of the gas-sensing mechanism is shown in Fig. 9.

4 Conclusion

The (Mn, Li)-co-doped ZnO gas sensors with varying Li concentrations were fabricated via sol-gel spin coating. Manganese and lithium were smoothly incorporated into the ZnO matrix to develop a superior, reliable, and selective NO₂ gas sensor. An XRD investigation confirmed the formation of a hexagonal wurtzite crystal structure and FESEM analysis verified spherical and irregular shaped grains with voids. XPS, UV-Visible spectroscopy, and PL studies also verified the presence of oxygen vacancies. Among them, ML-1 sample exhibits outstanding NO₂ gas sensitivity, excellent stability, exceptional selectivity, good repeatability, and rapid reaction and recovery times. Therefore, the incorporation of Li into Mn-doped ZnO results in a material that is potentially used in future gas-sensing applications.

Author contributions

KKJ contributed to Writing and preparation of original draft, sample synthesis, and Characterization. Dr. TAJ contributed to Resources, Methodology, Conceptualization, and Supervision. VSS contributed to Characterization. Dr. KNM contributed to Resources and Supervision. All authors reviewed the results and approved the final version of the manuscript.

Funding

The authors have not disclosed any funding.

Data availability

Data sharing does not apply to this article as no datasets were generated or analyzed during the current study.

Declarations

Competing interest The authors declare that they have no competing interests.

References

1. T. Tang, Z. Li, Y. Fen, H. Guang, X. Xing, Y. Li, J. Hazard. Mater. **451**, 131184 (2023)
2. X. Bai, H. Lv, Z. Liu, J. Chen, J. Wang, B. Sun, Y. Zhang, R. Wang, J. Hazard. Mater. **416**, 8 (2021)
3. K. Suganthi, E. Vinoth, L. Sudha, P. Bharathi, M. Navaneethan, Sens. Actuators B **380**, 133293 (2023)
4. B.M.A. Qureshi, N.J. Shah, C.W. Hemmen, M.C. Thill, Am. J. Crit. Care **12**, 147 (2016)
5. N. Sui, P. Zhang, T. Zhou, T. Zhang, Sens. Actuators B **336**, 129612 (2021)
6. B. Sharma, A. Sharma, J. Myung, Sens. Actuators B **331**, 129464 (2021)
7. X. Wang, T. Wang, G. Si, Y. Li, S. Zhang, X. Deng, X. Xu, Sens. Actuators B **302**, 127165 (2020)
8. H. Bai, H. Guo, J. Wang, Y. Dong, B. Liu, Z. Xie, F. Guo, D. Chen, R. Zhang, Y. Zheng, Sens. Actuators B **337**, 129783 (2021)
9. M.M. Gomaa, M.H. Sayed, V.L. Patil, M. Boshta, P.S. Patil, J. Alloys Compd. **885**, 160908 (2021)
10. M. Sik, M. Young, A. Mirzaei, H. Kim, S. Kim, S. Baek, D. Won, C. Jin, K. Hyoung, Appl. Surf. Sci. **568**, 150910 (2021)
11. T. Hsueh, S. Wu, Sens. Actuators B **329**, 129201 (2021)
12. S.D. Lokhande, M.B. Awale, V.D. Mote, J. Mater. Sci. Mater. Electron. **33**, 25063 (2022)
13. M.S.G. Selvan, K.K.M. Karunakaran, S.U.P. Baskaran, J. Electron. Mater. **51**, 2586 (2022)
14. V.S. Kamble, Y.H. Navale, V.B. Patil, N.K. Desai, S.N. Vajekar, J. Mater. Sci. Mater. Electron. **32**, 26503 (2021)
15. I.Y. Habib, A.A. Tajuddin, H.A. Noor, C.M. Lim, A.H. Mahadi, N.T.R.N. Kumara, Sci. Rep. Rep. **1**, 8 (2019)
16. M. Liu, Y. Shen, J. Mater. Sci. Mater. Electron. **34**, 1 (2023)
17. J. Zhao, C. Xie, L. Yang, S. Zhang, G. Zhang, Z. Cai, Appl. Surf. Sci. **330**, 126 (2015)
18. R.N. Mariammal, K. Ramachandran, Mater. Res. Express **8**, 79 (2018)

19. K.K. Jasmi, T.A. Johny, V.S. Siril, V. Kumar, K.N. Madhusoodanan, *Bull. Mater. Sci.* **0123456789**, 1 (2022)
20. D.K. Dubey, D.N. Singh, S. Kumar, C. Nayak, P. Kumbhakar, S.N. Jha, D. Bhattacharya, A.K. Ghosh, S. Chatterjee, *RSC Adv.* **6**, 22852 (2016)
21. C.W. Zou, H.J. Wang, M.L. Yi, M. Li, C.S. Liu, L.P. Guo, D.J. Fu, T.W. Kang, *Appl. Surf. Sci.* **256**, 2453 (2010)
22. C.W. Zou, L.X. Shao, L.P. Guo, D.J. Fu, T.W. Kang, *J. Cryst. Growth Cryst. Growth* **331**, 44 (2011)
23. N. Rajamanickam, R.N. Mariammal, S. Rajashabala, K. Ramachandran, *J. Alloys Compd.. Alloys Compd.* **614**, 151–164 (2014)
24. M.K.S.V. Kumar, *J. Mater. Sci. Mater. Electron.* **123**, 1–9 (2016)
25. T.A. Johny, V. Kumar, *J. Mater. Sci. Mater. Electron.. Mater. Sci. Mater. Electron.* **27**, 1456 (2014)
26. K.K. Jasmi, T.A. Johny, V.S. Siril, K.N. Madhusoodanan, *J. Sol-Gel Sci. Technol.. Sol-Gel Sci. Technol.* **8**, 1–12 (2023)
27. M.M. Elfaham, A.M. Mostafa, E.A. Mwafy, *J. Phys. Chem. Solids* **154**, 110089 (2021)
28. R. Nisha, Development of semiconductor metal oxide gas sensors for the detection of NO₂ and H₂S gases. *Material Science*, Cochin University of Science and Technology (2013)
29. M.S. Choi, M.Y. Kim, A. Mirzaei, H.S. Kim, S.I. Kim, S.H. Baek, D. Won Chun, C. Jin, K.H. Lee, *Appl. Surf. Sci.. Surf. Sci.* **568**, 150910 (2021)
30. V.L. Patil, S.A. Vanalakar, N.L. Tarwal, A.P. Patil, T.D. Dongale, J.H. Kim, P.S. Patil, *Sens. Actuators A* **299**, 111611 (2019)
31. C. Rajeev Gandhi, S. Bharanidharan, T. Jayakumar, N. Shailaja, P. Anand, *Solid State Commun. Commun.* **371**, 115256 (2023)
32. B. Gap, M. Zno, A. Khaleq, M. Alsmadi, B. Salameh, M. Shatnawi, *J. Phys. Chem. C* **124**, 29 (2020)
33. M.R. Islam, M. Rahman, S.F.U. Farhad, J. Podder, *Surf. Interfaces* **16**, 120 (2019)
34. D.E. Motaung, I. Kortidis, G.H. Mhlongo, M.-M. Duvenhage, H.C. Swart, G. Kiriakidis, S.S. Ray, *RSC Adv.* **6**, 31 (2016)
35. S. Rezaie, Z.G. Bafghi, N. Manavizadeh, *Int. J. Hydrogen Energy. J. Hydrogen Energy* **45**, 27 (2020)
36. S.A.V. Vhanalkar, V.L. Patil, S.M. Patil, S.B. Dhavale, T.D. Dongale, P.S. Patil, *J. Mater. Nanosci.* **9**, 13 (2022)
37. D.C. Reynolds, D.C. Look, B. Jogai, D.C. Reynolds, D.C. Look, B. Jogai, *J. Appl. Phys.* **6189**, 1 (2001)
38. M.E. Ashebir, G.M. Tesfamariam, G.Y. Nigussie, T.W. Gebreab, *J. Nanomater. Nanomater.* **3**(4), 93 (2018)
39. M. Shaheera, K.G. Girija, M. Kaur, V. Geetha, A.K. Debnath, R.K. Vatsa, K.P. Muthe, S.C. Gadkari, *Chem. Phys. Lett. Lett.* **758**, 137951 (2020)
40. C.H. Park, S.B. Zhang, S.H. Wei, *Phys. Rev. B. Rev. B* **66**, 1 (2002)
41. K. Rudra, Y.K. Prajapati, *Ceram. Int.* **46**, 8 (2020)
42. C. Belkhaoui, N. Mzabi, H. Smaoui, *Mater. Res. Bull.* **111**, 70–79 (2018)
43. Q. Shao, S. Qi, Y. Chen, O. Lam, Y. Yi, S. Foo, S.M. Ng, *J. Sol-Gel Sci. Technol.* **77**, 240 (2016)
44. S. Fabbiyola, L.J. Kennedy, A.A. Dakhel, M. Bououdina, J.J. Vijaya, T. Ratnaji, *J. Mol. Struct. Struct.* **1109**, 89–96 (2016)
45. S. Pramanik, S. Mondal, A.C. Mandal, S. Mukherjee, S. Das, T. Ghosh, R. Nath, M. Ghosh, P.K. Kuri, *J. Alloys Compd.* **849**, 156684 (2020)
46. K.K. Jasmi, T.A. Johny, V.S. Siril, N. Madhusoodanan, *Ind. J. Phys.* **8**, 1–10 (2023)
47. V.S. Kamble, R.K. Zemase, R.H. Gupta, B.D. Aghav, S.A. Shaikh, J.M. Pawara, *Opt. Mater. (Amst).* **131**, 112706 (2022)
48. V.S. Kamble, Y.H. Navale, V.B. Patil, N.K. Desai, S.T. Salunkhe, *J. Mater. Sci. Mater. Electron.* **32**, 2219 (2021)
49. R.S. Ganesh, V.L. Patil, E. Durgadevi, M. Navaneethan, S. Ponnusamy, C. Muthamizhchelvan, S. Kawasaki, P.S. Patil, Y. Hayakawa, *Chem. Phys. Lett.. Phys. Lett.* **15**, 136725 (2019)
50. N. Sun, Q. Tian, W. Bian, X. Wang, H. Dou, C. Li, *Appl. Surf. Sci.* **614**, 89 (2023)
51. W. An, X. Wu, X.C. Zeng, *J. Phys. Chem.* **112**, 5747 (2008)
52. M.J.S. Spencer, I. Yarovsky, *J. Phys. Chem. C* **3**, 10881 (2010)
53. M.G. Wardle, J.P. Goss, P.R. Briddon, *Phys. Rev. B* **71**, 15 (2005)
54. L. Zhang, Q. Fang, Y. Huang, K. Xu, P.K. Chu, F. Ma, Q. Fang, Y. Huang, K. Xu, P.K. Chu, F. Ma, *Anal. Chem.* **90**, 9821 (2018)
55. J. Han, A.M.R. Senos, P.Q. Mantas, *Mater. Chem. Phys.* **75**, 117 (2002)
56. M. Liu, A.H. Kitai, P. Mascher, *J. Lumin. Lumin.* **54**, 35 (1992)

Publisher's Note Springer Nature remains neutral with regard to jurisdictional claims in published maps and institutional affiliations.

Springer Nature or its licensor (e.g. a society or other partner) holds exclusive rights to this article under a publishing agreement with the author(s) or other rightsholder(s); author self-archiving of the accepted manuscript version of this article is solely governed by the terms of such publishing agreement and applicable law.